Food Hydrocolloids 106 (2020) 105912

Contents lists available at ScienceDirect

Food Hydrocolloids

journal homepage: www.elsevier.com/locate/foodhyd

Small angle neutron scattering quantifies the hierarchical structure in fibrous calcium caseinate

Bei Tian [a], Zhaojun Wang [b], Liliana de Campo [c], Elliot P. Gilbert [c,d,e], Robert M. Dalgliesh [f], Evgenii Velichko [a], Atze Jan van der Goot [b], Wim G. Bouwman [a,*]

[a] Department of Radiation Science and Technology, Delft University of Technology, The Netherlands
[b] Food Process Engineering, Wageningen University, The Netherlands
[c] Australian Centre for Neutron Scattering, Australian Nuclear Science and Technology Organisation, Locked Bag 2001, Kirrawee DC, NSW 2232, Australia
[d] Australian Institute for Bioengineering and Nanotechnology, The University of Queensland, Brisbane, QLD 4072, Australia
[e] Queensland Alliance for Agriculture and Food Innovation, The University of Queensland, Brisbane, QLD 4072, Australia
[f] ISIS Neutron and Muon Source, Science and Technology Facilities Council, Rutherford Appleton Laboratory, United Kingdom of Great Britain and Northern Ireland

ARTICLE INFO

Keywords:
Fibrous structure
Calcium caseinate
Small angle neutron scattering (SANS)
Anisotropic Guinier–Porod model
Mechanical property

ABSTRACT

Pronounced fibres are formed through simple shearing of a dense calcium caseinate dispersion. Both mechanical tests and scanning electron microscopy images demonstrate that the material is anisotropic. It is hypothesised that calcium caseinate aggregates, under shear, align into micro-fibres and bundle further into a hierarchical structure. Yet no direct evidence at the sub-micron length scale can support the assumption. Small angle neutron scattering (SANS) experiments were conducted on calcium caseinate samples prepared at different conditions. Analysis of the SANS data revealed that the micro-fibres have a diameter of ~100 nm and a length of ~300 nm. The addition of enzyme and air contributed to longer and thinner micro-fibres. Furthermore, the extent of fibre alignment at the micro-scale and the macroscopic anisotropy index followed the same trends with varying processing conditions. It is concluded that the material does indeed possess a hierarchical structure and the micro-fibres are responsible for the anisotropy on the macro-scale.

1. Introduction

A dietary transition towards more plant-based products can provide a long term solution to mitigate the impact of humans on the environment (De Boer & Aiking, 2011). However, this transition is severely hampered by the fact that the majority of consumers prefer animal-derived products to plant-based alternatives. Recent consumer research has shown that plant-based alternatives that effectively replicate meat structure could potentially stimulate the transition away from the consumption of meat (Elzerman, van Boekel, & Luning, 2013; Elzerman, Hoek, Van Boekel, & Luning, 2011; Hoek, Luning, Weijzen, Engels, Kok, & De Graaf, 2011), thus emphasising the importance of fibrous structures in meat analogues.

Over the years, a variety of meat analogues have been developed using different ingredients and through different technologies (Apichartsrangkoon, 2002; Asgar, Fazilah, Huda, Bhat, & Karim, 2010; Dekkers, Hamoen, Boom, & van der Goot, 2018; Finnigan, Needham, & Abbott, 2017; Nieuwland et al., 2013; Owusu-Ansah & McCurdy, 1991; Peighambardoust, Van der Goot, Hamer, & Boom, 2004). One prominent candidate is calcium caseinate (Manski, van Riemsdijk, van der Goot, & Boom, 2007b). It is obtained by re-dissolving the acid casein curd in a $Ca(OH)_2$ solution (Fuquay, McSweeney, & Fox, 2011), then subjected to drying. Given the vigorous processing condition, the structure of calcium caseinate has become different from that of casein micelles. According to previous studies (HadjSadok, Pitkowski, Nicolai, Benyahia, & Moulai-Mostefa, 2008; Smialowska, Matia-Merino, Ingham, & Carr, 2017; Thomar, Gonzalez-Jordan, Dittmer, & Nicolai, 2017; Thomar, Nicolai, Benyahia, & Durand, 2013), the structure of calcium caseinate in solution is somewhat comparable to that of adding Ca^{2+} ions to sodium caseinate. Below a critical calcium concentration, the system mainly comprises small caseinate clusters, with a radius of ~10 nm. Above that, which is the case of calcium caseinate used in our study, larger aggregates are formed and the structure becomes rather compact and heterogeneous. Thus, it is reasonable to assume that calcium caseinate aggregates behave as interacting particles that are composed of sub-aggregates made of small protein clusters. Under simple shear and mild heat, a 30%w/w calcium caseinate dispersion can be transformed into pronounced fibrous structure. Scanning electron microscopy (SEM) images have shown that caseinate aggregates, with

* Corresponding author.
E-mail address: W.G.Bouwman@tudelft.nl (W.G. Bouwman).

https://doi.org/10.1016/j.foodhyd.2020.105912
Received 18 November 2019; Received in revised form 6 March 2020; Accepted 1 April 2020
Available online 8 April 2020

a typical diameter of a few hundreds of nanometres, are aligned into fibres which are parallel to the shear flow direction (Manski, van der Goot, & Boom, 2007). Given these fibres are also visible to the eye, it is hypothesised that the fibrous calcium caseinate has a hierarchical structure which prevails from mili-down into the nanometre length scale.

Based on this hypothesis, research has been conducted to study the anisotropy of fibrous calcium caseinate (Grabowska, van der Goot, & Boom, 2012; Tian, Wang, van der Goot, & Bouwman, 2018). The current understanding is that air bubbles are present in the protein dispersion during pre-mixing and that they enhance the anisotropy of the final material (Wang, Tian, Boom, & van der Goot, 2019a). The addition of a crosslinking enzyme, transglutaminase, also appears to improve the anisotropy, as does maltodextrin (Wang, Dekkers, Boom, and van der Goot, 2019). In the above studies, the occurrence and quantification of anisotropy have always been examined by mechanical tests. The anisotropy index is calculated as the ratio between the true stress (or fracture strain) of the material being fractured parallel or perpendicular to the shear flow direction. As informative as the mechanical test can be, it is a bulk measurement that reflects the property of the material on the macroscopic scale; thus, a direct method that can prove and quantify the anisotropy and structure of the fibres at the microscopic scale is desirable.

The small angle neutron scattering (SANS) technique is proposed to serve this role in the study of the structure of the fibres. Small angle X-ray scattering is also a powerful method, given its shorter measurement time and smaller sample size required. Yet, neutrons are used in this study for two reasons. One is that due to the heterogeneity of the sample, a larger beam size required by SANS actually provides an 'advantage' of probing a more representative volume of samples processed at different conditions. The other reason is that complementary ultra-small angle neutron scattering (USANS) studies were originally conducted within the same facility. However, the intrinsic anisotropy of the sample combined with the slit-smeared data collection mode, added even more complexity beyond what already evident is in the SANS region. As a result, the USANS data are not discussed in this study.

SANS has been successfully applied to study the anisotropy and structure of many materials at the microscopic scale, such as the shear-induced orientation of polymer clay platelets (Schmidt, Nakatani, Butler, & Han, 2002), the chain conformation of model inter-penetrated elastomer networks (Ducrot, Montes, & Creton, 2015), the orientation of collagen in human dentine (Kinney, Pople, Marshall, & Marshall, 2001), the hierarchical structure of bacterial cellulose (Martínez-Sanz, Mikkelsen, Flanagan, Gidley, & Gilbert, 2017) and the structural transitions in fibrin networks under shear deformation (Weigandt, Porcar, & Pozzo, 2011). The application of SANS on food materials has also grown in recent years (Gilbert, 2019; Lopez-Rubio & Gilbert, 2009). It has contributed to a better understanding of the hierarchical structure of plant cell walls (Martínez-Sanz, Gidley, & Gilbert, 2015) and to the characterisation of starch structure (Blazek & Gilbert, 2011). Similar to these studies, we expect a connection between the dimensions and anisotropy of the fibres obtained from SANS and the bulk mechanical properties.

In this work, SANS experiments were carried out on calcium caseinate samples following production at different shearing rates and times, both with or without the inclusion of enzyme and air. An analysis of the annular intensity was performed to quantify the extent of fibre alignment at the micro-scale; a combined Guinier–Porod model was applied to fit two perpendicular sector intensities so as to extract the structural information of the micro-fibres. The SANS results were then compared to those obtained from mechanical tests.

2. Experimental section

2.1. Preparation of the fibrous materials

2.1.1. Materials

Spray-dried calcium caseinate powder was kindly provided by DMV International (Veghel, the Netherlands). According to the manufacturer's specification, it contains 91.5%w/w protein, ~ 5.2%w/w moisture and 3.9%w/w ash, among which 1.5%w/w is calcium. In practice, the measured dry matter is 94.8%w/w.

The activity of the microbial Ca^{2+}-independent transglutaminase derived from the Streptoverticillium moberansae (1%w/w transglutaminase, 99%w/w maltodextrin; Ajinomoto Co. Inc., Tokyo, Japan) is 114 units·g^{-1}, determined by the hydroxamate method (Yokoyama et al., 2003). A 20%w/w (in demineralised water) transglutaminase solution is stirred at room temperature for 1 h.

2.1.2. Preparation of the protein dispersions

Samples without enzyme or air were prepared from de-aerated protein dispersions before being loaded into a shear cell device (Van der Zalm, Berghout, Van der Goot, & Boom, 2012). A protein dispersion is obtained through manually mixing 30 g of calcium caseinate powder with 70 g of demineralised water using a spatula. The dispersion was then heated at 80 °C for 5 min and centrifuged at 2500 × g for 2 min to remove most of the air. It was left at room temperature for 55 min before being transferred to the shear cell device. Samples with enzyme and air were prepared by manually mixing 30 g of protein powder with 62.5 g of water and 7.5 g of transglutaminase solution for 1 min.

2.1.3. Structure formation in the shear cell device

Well-defined shear flow was applied to the protein dispersion using a custom built shearing device (Wageningen University, the Netherlands). It consists of a rotating cone (the bottom cone, angle = 105°) and a stationary cone (the top cone, angle = 100°). More details are described in earlier publications (Van der Goot, Peighambardoust, Akkermans, & van Oosten-Manski, 2008; Van der Zalm et al., 2012). Both cones were thermostatted with a circulating water bath.

The protein dispersions were transferred to the pre-heated (50 °C) shear cell device after mixing. The dispersions without enzyme or air were then subjected to shear at various rates (40, 50, 75, 100, 125 and 150 rpm) for 5 min. The dispersions with enzyme and air were subjected to either various shear rates (10, 25, 75, or 150 rpm) for 5 min, or to various shear times (1, 2.5, 15 or 30 min) at 50 rpm. After processing, the materials were cooled for 10 min at 4 °C. Tensile tests were performed within 1 h after removal of the material from the shear cell device. Parts of the materials were stored at −20 °C prior to the SANS measurements.

The material sheared for 30 min showed phase separation (Grabowska et al., 2012). The area that was close to the tip of the shear cell was a uniform, yellowish gel, whereas the area close to the edge remained fibrous. Only the fibrous part was measured by the tensile test while both the fibrous and gel parts were measured by SANS. The resultant sector intensities of the fibrous part were fitted with a combined Guinier–Porod model, while the isotropic scattering from the gel part was compared to a sample without shear.

2.2. Tensile strength analysis

To study the mechanical property of the fibrous material, a texture analyser (Instron Testing System, table model 5564) was used with a load cell of 100 N. A dog bone shaped mould was used to cut the material. A detailed preparation procedure can be found elsewhere (Wang, Dekkers, Boom, and van der Goot, 2019). The sample was 15.2 mm long and 3.18 mm wide, its thickness varied from 4 to 6 mm. The material was cut both parallel and perpendicular to the shear flow direction (based on the shear-vorticity plane). Tensile tests were conducted at

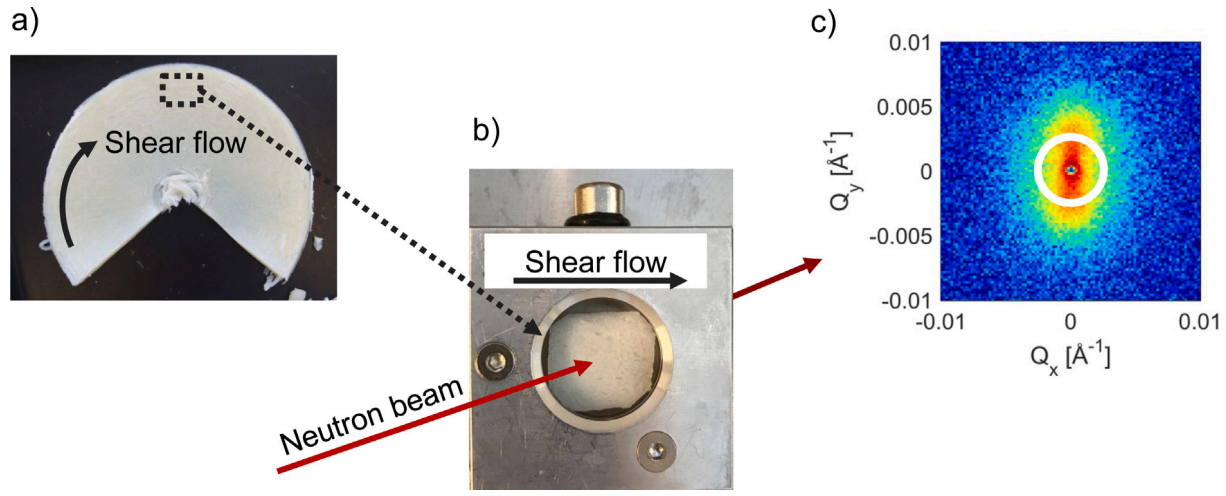

Fig. 1. An illustration of the sample preparation for the SANS measurements. (a) a rectangular sample ($L \times H \times W \approx 1 \times 0.7 \times 0.2$ cm) was cut from a fibrous gel slab, with its length being parallel to the shear flow direction. (b) this sample was placed in a sample holder and presented to the neutron in transmission geometry. (c) a typical 2D scattering pattern obtained using the focusing configuration on the QUOKKA instrument.

a constant deformation speed of 3 mm/s. Grips with abrasive paper were used to prevent slippage during the test. At least three specimens per direction were measured. The results were depicted as force–displacement curves. The true stress (σ, kPa) and the Hencky strain (ε, -) were calculated as $\sigma = F(t)/A(t)$ and $\varepsilon = ln(L(t)/L_0)$, where $F(t)$ is the force, $A(t)$ is the cross sectional area, $L(t)$ is the length of the sample at time t, and L_0 is the initial length of the tensile bar (15.2 mm).

The Young's modulus ($E = \sigma/\varepsilon$, kPa) was calculated by applying a linear fit to the initial displacement. A Hencky strain interval between 0.03–0.27 was taken. The macroscopic anisotropy index was calculated as $E_{\parallel}/E_{\perp}$, where $E_{\parallel}$ is the Young's modulus of the sample fractured in the direction parallel to the shear flow, and $E_{\perp}$ is perpendicular to the shear flow.

2.3. Small angle neutron scattering (SANS)

SANS experiments of materials processed through the shear cell device were performed at the OPAL reactor, Australian Nuclear Science and Technology Organisation (ANSTO). Fig. 1 illustrates how a sample was cut from the material and mounted for the neutron measurement. Samples without enzyme or air were measured on the pinhole QUOKKA instrument (Gilbert, Schulz, & Noakes, 2006; Wood et al., 2018). Four configurations were used to cover a Q range of 0.0006 to 0.64 Å^{-1}, where Q is the magnitude of the scattering vector defined as $Q = (4\pi/\lambda)\sin\theta$, λ is the wavelength in Å and 2θ is the scattering angle. The four configurations were: (i) source-to-sample distance (SSD) = 20.2 m with focusing optics using MgF_2 lenses; (ii) SSD = 20.2 m, sample-to-detector distance (SDD) = 20.1 m; (iii) SSD = 8.0 m, SDD = 8.0 m and (iv) SSD = 12 m, SDD = 1.3 m, with 10% wavelength resolution and λ = 8.1 Å for (i) and λ = 5.0 Å for (ii)–(iv). Source and sample apertures of 50 mm and 12.5 mm were used respectively. Sample temperature was controlled by a Huber thermostatted bath and held at 25 °C throughout the measurements. All data were corrected for blocked beam measurements, normalised, radially averaged and placed on an absolute scale, following attenuated direct beam measurements, using a package of macros in the Igor Pro software (Wavemetrics, Lake Oswego, OR, U.S.A.) modified to accept HDF5 data files from QUOKKA. Fig. 2 gives an example on how sector cut intensities, obtained at different SDD, were combined into 1D sector intensities. To correct for the incoherent scattering from the solvent, 70% of the scattering intensity of the H_2O was subtracted from each sample.

Samples with enzyme and air were measured on the BILBY instrument (Sokolova et al., 2019). A wavelength range of 2–20 Å yielded a Q range of 0.001 to 0.35 Å^{-1}, which is similar to QUOKKA. The BILBY data were reduced using the Mantid framework (Arnold et al., 2014). A different background subtraction approach was taken to correct for the incoherent scattering. The slope of the scattering curve at high Q was fitted with the sum of a constant and a power law, the percentage of the H_2O subtracted from the sample was determined by the value of the fitted constant.

One reference sample–the protein dispersion without shear–was measured on the LARMOR instrument at ISIS, UK. The time-of-flight instrument utilised wavelength of 0.9 to 13 Å, which gave a Q range of 0.003–0.4 Å^{-1}. To account for the incoherent background, 70% of the scattering intensity of the H_2O was subtracted. Data reduction was performed using the Mantid framework (Arnold et al., 2014).

The vertical sector intensity was obtained by averaging over ±10° along the direction where the intensity is the highest. The horizontal sector intensity was obtained by averaging the intensity over ±10° in the direction perpendicular to the highest intensity. The vertical and horizontal sector intensities were fitted simultaneously using a combined Guinier–Porod model (Eqs. (2) and (3)). This was achieved by embedding the model as a plugin function into the simultaneous fit functionality of SASView 4.2.0 (Doucet et al., 2017).

3. Results and discussion

3.1. Size and structure of the calcium caseinate gel

3.1.1. Size and structure of the caseinate particle in the unsheared protein dispersion

The two perpendicular sector intensities of the unsheared protein dispersion shown in Fig. 3a overlap, confirming that the material is isotropic. The scattering intensity continues to increase in the limit of low Q of the instrument, suggesting the presence of larger aggregates or clusters in the gel. Some large aggregates are indeed observed in the SEM image presented in Fig. 4a.

An empirical 'broad peak' model (Doucet et al., 2017) is applied to fit the isotropic scattering data. This model can describe not only scattering features such as a small bump at ~0.02Å^{-1} in Fig. 3a, but also features such as a sharper peak in Fig. 3d (the gel part of the phase separated sample). It offers the advantage that fitted parameters from different samples are consistent and comparable, which is not possible for other models with less fitting parameters. The 'broad peak' model is given by

$$I(Q) = \frac{A}{Q^{d_0}} + \frac{C}{1 + (|Q - Q_0|\xi)^m} + \text{Background}, \quad (1)$$

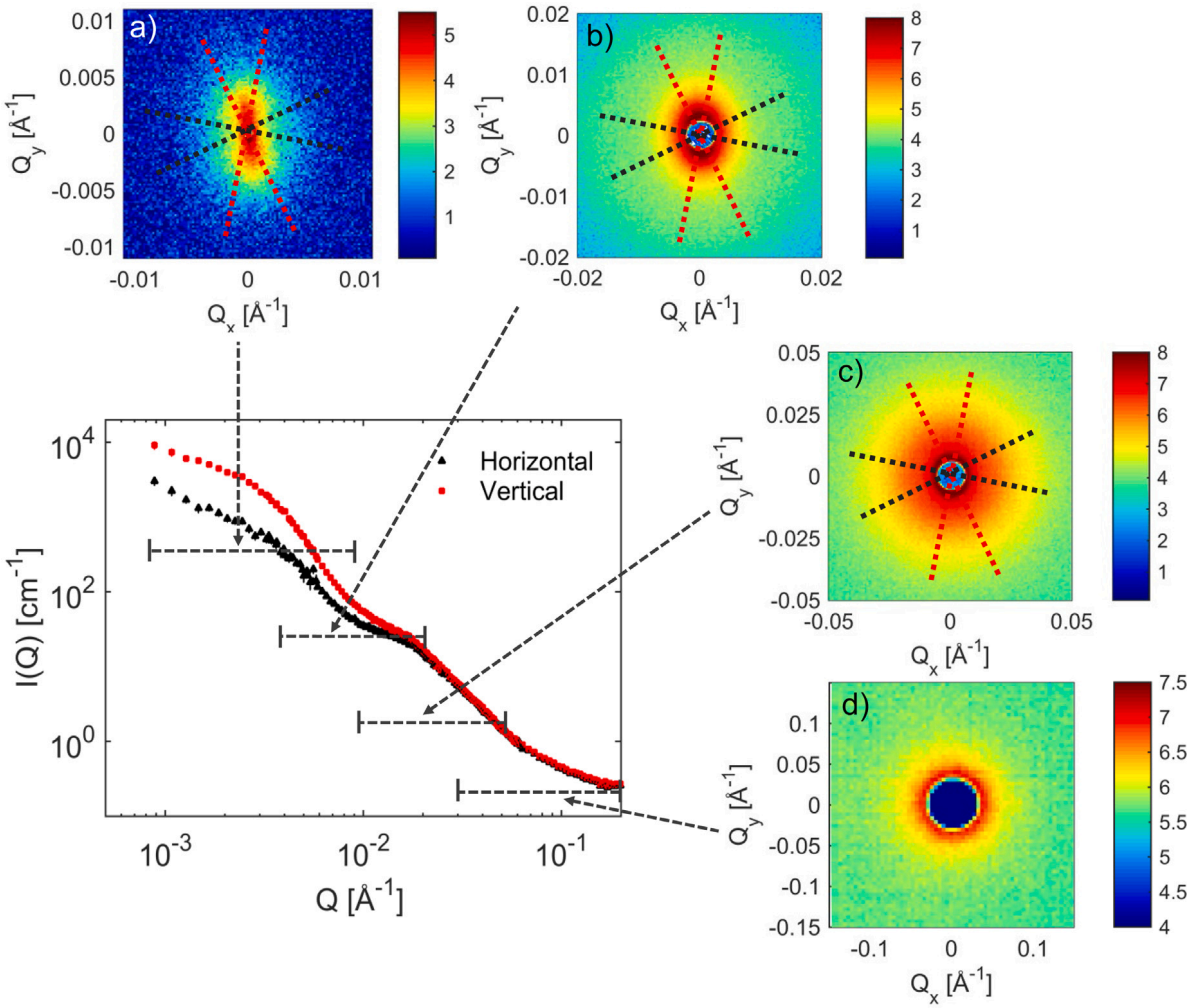

Fig. 2. A complete set of the reduced and normalised sector intensities of a sample (without enzyme or air, sheared at 75 rpm for 5 min) measured on the QUOKKA instrument. Data were obtained by combining four instrument configurations that each covers a Q range (indicated by dashed lines). Figs. (a)–(d) are 2D scattering patterns from the corresponding lens with detector at 20 m, conventional 20 m, 8 m and 1.3 m detector positions. The 2D patterns are presented as measured.

Table 1
Fitted parameters of the isotropic protein gel using the model from Eq. (1).

	A	d_0	C	m	Q_0 [Å^{-1}]	ξ [nm]
1[a]	(4.0 ± 2.4)×10^{-7}	3.8 ± 0.1	19.3 ± 0.8	2.0 ± 0.1	0.013 ± 0.001	9.8 ± 0.3
2[b]	(3.4 ± 0.3)×10^{-5}	2.6 ± 0.1	3.7 ± 0.1	1.0 ± 0.1	0.040 ± 0.001	3.7 ± 0.1

[a]Protein dispersion without shear (Fig. 3a).
[b]Sheared for 30 min (gel part in Fig. 3d).

where A and d_0 is the Porod scale factor and the exponent respectively; C and m is the Lorentzian scale factor and the exponent respectively; ξ is the Lorentzian screening length, which can be interpreted as the gel mesh size in case of a gel network (Saffer, Lackey, Griffin, Kishore, Tew, & Bhatia, 2014). The peak position Q_0 is related to the d-spacing as $d = 2\pi/Q_0$, which corresponds to the average centre-to-centre distance between neighbouring particles (Curtis, McAuley, Nanda, & Krueger, 2012).

Fitted parameters of the sample without shear (Fig. 3a) are presented in the first row in Table 1. The d-spacing between the neighbouring particles is approximately 48 nm, the mesh size of the gel is around 10 nm, which seems to be in agreement with the small sphere-like particles shown in Fig. 4a. In the case of caseinate, this gel mesh size may be interpreted as the size of a sub-aggregate, since it is close to the average value of the substructure in casein micelles (Dalgleish, Spagnuolo, & Goff, 2004; Ingham et al., 2016; Stothart & Cebula, 1982). Furthermore, this size is also similar to the radius of gyration (R_g) of the sphere-like particles in the fibrous samples without enzyme or air shown in Table 2, suggesting that these sub-aggregates are the elementary building block in caseinate.

The 'broad peak' model is also applied to fit the gel part of the phase separated sample shown in Fig. 3d, the resultant fitted parameters are presented in the second row in Table 1. The gel mesh size is reduced to less than one half of that compared to the protein dispersion without shear, as is the d-spacing. This may be explained as the caseinate sub-aggregates becoming compacted over time. Expelled water is observed on the surface of the gel after 30 min of shearing, which supports this explanation. Because the compacted particles are denser than the fibres, the material phase separates into a dense isotropic gel that is close to the tip of the cone and a fibrous gel close to the edge.

3.1.2. Size and structure of the fibres in anisotropic protein dispersions

The SEM image in Fig. 4b reveals that the sheared sample contains cylinder-like micro-fibres which are composed of sphere-like aggregates. A schematic illustration is presented in Fig. 4c. We propose the following empirical 2D model to fit the anisotropic scattered intensity.

$$\begin{aligned} I(Q,\alpha) &= I_{\text{fibre}}(Q,\alpha) + I_{\text{sphere}}(Q) + \text{Background} \\ I_{\text{fibre}}(Q,\alpha) &= G_f \cdot F_l(Q,\alpha) \cdot F_r(Q,\alpha) \\ I_{\text{sphere}}(Q) &= G_s \cdot F_s(Q) \end{aligned} \tag{2}$$

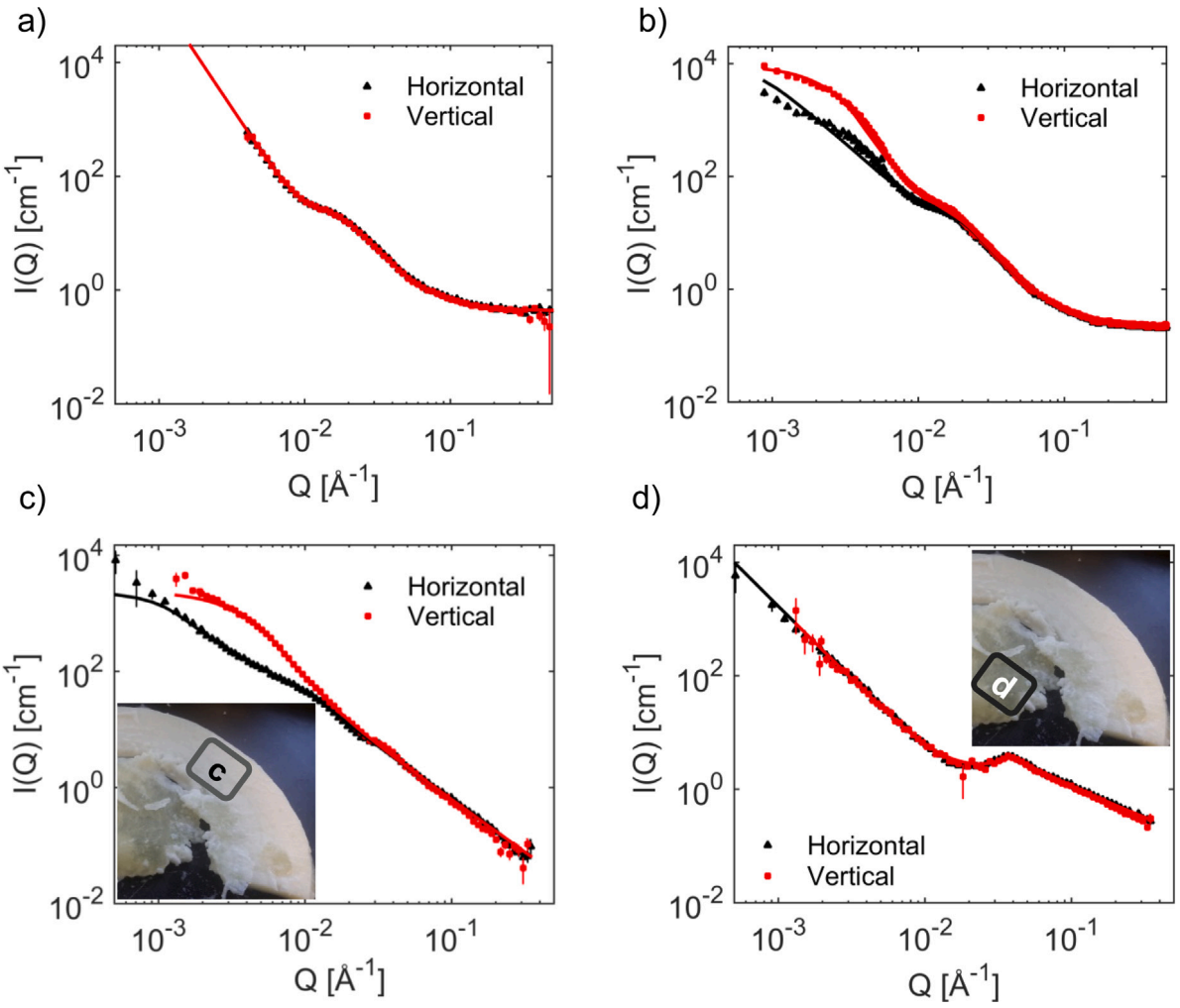

Fig. 3. Examples of typical sector scattering from different samples. (a) an unsheared protein dispersion; (b) a fibrous sample sheared at 75 rpm for 5 min, without enzyme or air; (c) the fibrous part (inset) of a sample sheared at 50 rpm for 30 min, with addition of enzyme and air; (d) the gel part (inset) of the same sample as (c). Lines in (a) and (d) represent fits using a broad peak model, lines in (b) and (c) are fits of the sector intensities using a combined Guinier–Porod model.

where

$$F_l(Q,\alpha) = \begin{cases} e^{\frac{-(Q\cdot\cos\alpha\cdot L)^2}{12}} & Q \le \frac{\sqrt{12}}{L\cdot\cos\alpha} \\ \left(\frac{\sqrt{12/e}}{Q\cdot\cos\alpha\cdot L}\right)^2 & Q \ge \frac{\sqrt{12}}{L\cdot\cos\alpha} \end{cases}$$

$$F_r(Q,\alpha) = \begin{cases} e^{\frac{-(Q\cdot\sin\alpha\cdot D)^2}{12}} & Q \le \frac{\sqrt{18}}{D\cdot\sin\alpha} \\ \left(\frac{\sqrt{18/e}}{Q\cdot\sin\alpha\cdot D}\right)^3 & Q \ge \frac{\sqrt{18}}{D\cdot\sin\alpha} \end{cases} \quad (3)$$

$$F_s(Q) = \begin{cases} e^{\frac{-(Q\cdot R_g)^2}{3}} & Q \le Q_1 \\ \frac{D_s}{Q^d} & Q \ge Q_1 \end{cases}$$

In Eq. (2), $I_{\text{fibre}}(Q,\alpha)$ describes the anisotropic scattering from the cylinders, G_f is a pre-factor. Given the system contains 30%w/w protein, it is jammed rather than dilute, which means G_f is only proportional but not equal to the product of the volume, volume fraction and the square of the scattering length density contrast of the micro-fibres. As a result, G_f will be fitted as an additional parameter. The isotropic scattering from the spheres is described by $I_{\text{sphere}}(Q)$ (Hammouda, 2010). Similar to G_f, G_s is the pre-factor for the scattering from the spheres. In Eq. (3), L and D are the length and diameter of the cylinder, respectively, R_g is the radius of gyration of the sphere and d is the Porod exponent which describes the roughness of the surface; $Q_1 = \frac{1}{R_g}\sqrt{\frac{3d}{2}}$ and $D_s = e^{\frac{-(Q_1\cdot R_g)^2}{3}}\cdot Q_1^d$.

The angle α specifies the scattering intensity in a certain direction. α_x and α_y are the angles between the cylinder axis and the x-axis or y-axis on the detector plane, respectively. During measurements the fibres are placed parallel to the x-axis, thus the horizontal intensity is obtained at $\alpha_x = 0°$ and the vertical intensity is obtained at $\alpha_y = 90°$. Due to the complexity and heterogeneity of the sample, both the orientation and sizes of the micro-fibres are expected to be polydispersed. Yet, the size distribution is not included because models in Eq. (3) do not contain any sharp interference features which form factors of cylinders or spheres have; this means fitted dimensions of the fibres will represent an average value of the system. As a result, only a Gaussian distribution for both α_x and α_y is included, with a standard deviation of 20°.

The two perpendicular sector intensities are fitted simultaneously using Eqs. (2) and (3). Fig. 3b displays the sector intensities and the corresponding fits of a sample without enzyme or air, and Fig. 3c shows the data and fits of a sample with the addition of enzyme and air. The rest of the data and their corresponding fits can be found in the supplementary information. The slight inconsistency between the fits and the data at low Q from the BILBY data may have risen from the multiple scattering from the sample. Dimensions of the micro-fibres at

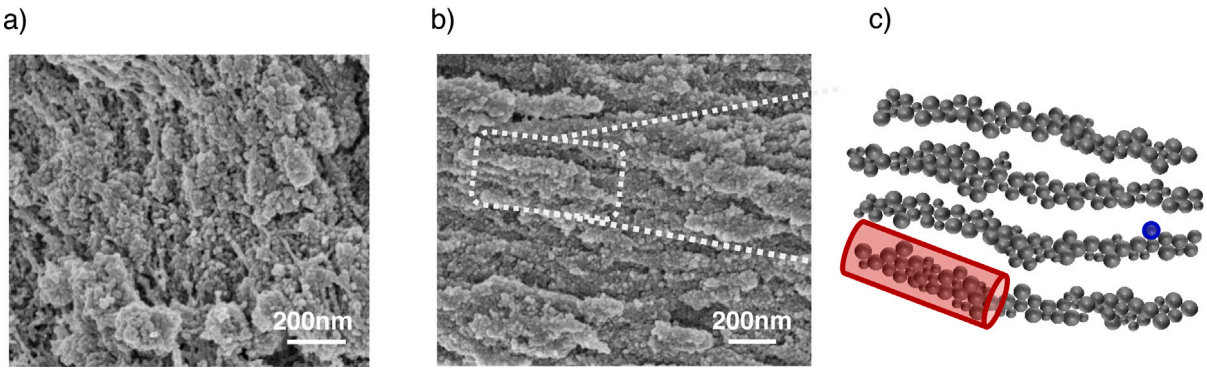

Fig. 4. An illustration of the fibres based on SEM images. (a) a SEM image of the protein dispersion without shear. Sub-aggregates with a diameter of ~10 nm form larger sphere-like aggregates with a size of a few hundreds of nanometres. (b) Reproduction of a SEM image of a sheared sample (without enzyme or air, sheared at 50 rpm for 5 min) fractured parallel to the shear flow direction (Wang et al., 2019a). Copyright 2019, Elsevier. (c) A schematic illustration of the micro-fibres: the system can be simplified into cylinders composed of sphere-like calcium caseinate aggregates.

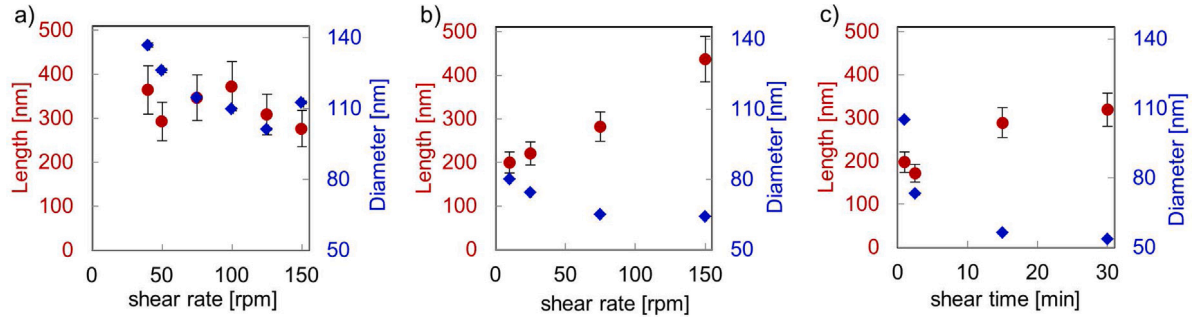

Fig. 5. Fitted length (red circles) and diameter (blue diamonds) of the micro-fibres as a function of shear rate or time. (a) samples without enzyme or air, sheared at 40, 50, 75, 100, 125 and 150 rpm for 5 min. (b) samples with enzyme and air, sheared at 10, 25, 75 and 150 rpm for 5 min. (c) samples with enzyme and air, sheared at 50 rpm for 1, 2.5, 15 and 30 min. The error bar of the diameter is smaller than the size of the symbol.

Table 2
A summary of the fitted parameters of the sector intensities using the model from Eqs. (2) and (3).

No enzyme or air	R_g [nm]	G_f [10^{-12} Å^{-4}]	G_s [10^{-12} Å^{-4}]	d	bkgd [cm^{-1}]
40 rpm	8.3 ± 0.1	0.17 ± 0.01	0.40 ± 0.01	2.74 ± 0.01	0.31 ± 0.01
50 rpm	8.6 ± 0.1	0.16 ± 0.01	0.39 ± 0.01	2.72 ± 0.01	0.31 ± 0.01
75 rpm	8.2 ± 0.1	0.16 ± 0.01	0.39 ± 0.01	2.72 ± 0.01	0.22 ± 0.01
100 rpm	8.5 ± 0.1	0.18 ± 0.01	0.41 ± 0.01	2.70 ± 0.01	0.50 ± 0.01
125 rpm	8.4 ± 0.1	0.17 ± 0.01	0.38 ± 0.01	2.65 ± 0.01	0.23 ± 0.01
150 rpm	8.5 ± 0.1	0.16 ± 0.01	0.39 ± 0.01	2.69 ± 0.01	0.30 ± 0.01
With enzyme & air	R_g [nm]	G_f [10^{-12} Å^{-4}]	G_s [10^{-12} Å^{-4}]	d	bkgd [cm^{-1}]
10 rpm	15.2 ± 0.1	0.17 ± 0.01	0.28 ± 0.01	2.03 ± 0.01	0.39 ± 0.01
25 rpm	13.3 ± 0.1	0.15 ± 0.01	0.27 ± 0.01	1.96 ± 0.01	0.21 ± 0.01
75 rpm	13.1 ± 0.1	0.16 ± 0.01	0.26 ± 0.01	1.81 ± 0.01	0.01 ± 0.01
100 rpm	14.8 ± 0.1	0.17 ± 0.01	0.26 ± 0.01	2.03 ± 0.01	0.02 ± 0.01
With enzyme & air	R_g [nm]	G_f [10^{-12} Å^{-4}]	G_s [10^{-12} Å^{-4}]	d	bkgd [cm^{-1}]
1 min	11.6 ± 0.1	0.15 ± 0.01	0.29 ± 0.01	2.04 ± 0.01	0.24 ± 0.01
2.5 min	5.4 ± 0.1	0.09 ± 0.01	0.33 ± 0.01	1.79 ± 0.01	0.03 ± 0.01
15 min	11.9 ± 0.1	0.14 ± 0.01	0.21 ± 0.01	1.73 ± 0.01	0.12 ± 0.01
30 min (fibre-part)	7.6 ± 0.1	0.21 ± 0.01	0.27 ± 0.01	1.41 ± 0.01	0.06 ± 0.01

different shearing conditions are shown in Fig. 5; the rest of the fitted parameters are summarised in Table 2.

As shear rate increases, the diameter of the fibre in samples without enzyme or air (Fig. 5a) first decreases from 137 ± 1 to 101 ± 1 nm and then increases to 113 ± 1 when the shear rate is higher than 125 rpm. The length of the fibre is ~320 nm and remains nearly constant. The highest aspect ratio (=L/D) is obtained in the sample sheared at 100 rpm. Samples with the addition of enzyme and air contain slightly longer and much thinner micro-fibres. Fig. 5b shows that the length increases from ~200 to ~450 nm while the diameter decreases from ~80 to ~65 nm with increasing shear rate. A longer shear time has a similar but more severe impact on the diameter. It is reduced to one half after being sheared for more than 15 min, as shown in Fig. 5c. The increase in the length of the micro-fibre can be attributed to the crosslinking by tranglutaminase. Yet, what contributes more to the higher aspect ratio of the micro-fibres in Fig. 5b and c is the drastic reduction in the diameter. This is probably due to the incorporation of air. Elongated air bubbles compact the material, especially in the direction perpendicular to the shear flow, thus leading to the decrease in the diameter.

As mentioned before, the sphere-like aggregates in the micro-fibres are composed of elementary sub-aggregates. The R_g of these sub-aggregates is equal to ~8.5 nm in samples without enzyme or air (first column in Table 2). This size remains constant with increasing shear

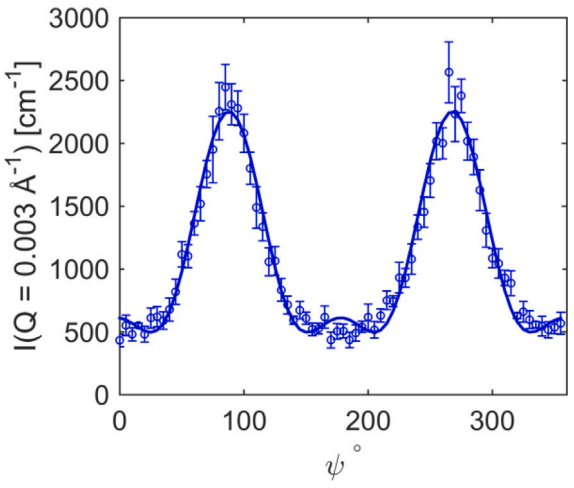

Fig. 6. An example of the annular intensity fitted with the Legendre polynomial. A small bump at ~180° is likely to be caused by the higher order Legendre polynomial.

rate, indicating that shear merely aligns the larger aggregates and has no influence on the sub-structure of the caseinate. This has also been observed by Jaspe and Hagen (2006) in a modelling study, which concludes that an extremely high shear rate (~10^7 s^{-1}) is required before shear takes effect in the shape or structure of the protein particle. On the other hand, the R_g in samples with enzyme and air nearly doubled. This implies that the enzyme not only extends the length of the fibre but also crosslinks the sub-aggregates which consequently contributes to stronger fibres.

The fitted G_f and G_s in Table 2 remain nearly constant within each sample set, indicating that processing conditions have little to no influence on the SLD contrast and the volume fraction. Even so, it remains challenging to identify the exact cause of the SLD contrast, due to the complexity of the system. For instance, both the SLD contrast between the fibres and the air and the contrast between the fibres and the solvent contribute to the G_f. It is thus concluded that even though values of G_f and G_s are in agreement with the composition of the protein, the results remain phenomenological.

3.2. Extent of fibre alignment

The annular intensity obtained from the 2D pattern provides information on the extent of fibre alignment and the orientation of the fibres with respect to the shear flow direction. Fig. 3b and c shows that the intensity begins to diverge at $Q < 0.01$ Å^{-1}. As a result, the annular intensity at $Q = 0.003$ Å^{-1} is plotted and fitted with the Legendre polynomial (Burger, Hsiao, & Chu, 2010; Weigandt et al., 2011)

$$I(Q = 0.003\text{Å}^{-1}, \psi) = \sum_{n=0}^{\infty} a_n \cdot P_{2n}(\cos\psi^*) \quad (4)$$

where a_n is the pre-factor of the polynomial, $\psi^* = \psi - (\psi_0 + \frac{\pi}{2})$, ψ_0 is the angle between the average direction of the fibres and the shear flow. It is also the direction at which the scattering intensity is the highest. Fig. 6 gives an example of the goodness of the fit.

The micro-fibres' extent of alignment is related to the Hermans' orientation or nematic order parameter (Hermans, Hermans, Vermaas, & Weidinger, 1946), and is calculated as $\frac{a_1}{5a_0}$. When $\frac{a_1}{5a_0} = 1$, the system has a perfect parallel orientation; when $\frac{a_1}{5a_0} = 0$, the system is totally randomly oriented, and $\frac{a_1}{5a_0} = -0.5$ when the system has a perfect perpendicular orientation (Burger et al., 2010; Weigandt et al., 2011). Given all the samples were mounted with the shear flow direction being parallel to the x-axis on the detector plane, $\frac{a_1}{5a_0}$ should have values between 0 and 1.

Fig. 7 summarises the extent of alignment from different samples. For samples without enzyme or air, the extent of alignment first increases with shear rate and then decreases. The most anisotropic fibre is produced between 75 and 100 rpm. The higher shear rate accompanied by the larger shear stress could break up the alignment of the micro-fibres (Wang, Tian, Boom, and van der Goot, 2019b), thus leading to the decrease in the extent of alignment. As for samples with enzyme and air, a continuous increase in the extent of alignment is observed when increasing either shear rate or time. Such a trend is also observed in the aspect ratio of the micro-fibres. Compared to samples without enzyme or air, the extent of alignment in samples with enzyme and air is greater at higher shear rate, and the micro-fibres have already shown alignment at shear rates lower than 40 rpm.

To summarise, through analysing the SANS data, we have gained insights into the sizes, structure and extent of alignment of the micro-fibres in calcium caseinate gels. Enzyme and air enhanced the orientation of the micro-fibres and facilitated systematic manipulation (e.g. varying shear rate or time) of the dimensions of the micro-fibres.

3.3. Mechanical properties

Several parameters can describe the macroscopic anisotropy, such as the true stress, Hencky strain or Young's modulus. The true stress and Hencky strain are determined by the fracture point where a drastic decrease of the stress is observed in the stress–strain curve. These measurements can distinguish well the trend in the macroscopic anisotropy but are not comparable to the microscopic anisotropy derived from SANS. The reason is that the material is fractured irreversibly, while no deformation is applied to the sample during the SANS measurement.

Perhaps a more appropriate indication of the macroscopic anisotropy is the Young's modulus. It describes the stiffness of the material and is calculated using the near-zero linear region of the stress–strain curve. This method ensures the deformation is elastic, reversible and kept to a minimum. It should also be noted that the anisotropy index obtained this way is expected to be smaller than the reported anisotropy indices calculated from the true stress or Hencky strain (Wang, Tian, Boom, and van der Goot, 2019b), due to the fact that a smaller stress–strain region is employed.

The macroscopic anisotropy index together with the Young's moduli of samples fractured in the direction parallel or perpendicular to the shear flow are presented in Fig. 8. For samples without enzyme or air, $E_{\parallel}$ and $E_{\perp}$ remain nearly constant with increasing shear rate, as is the resultant macroscopic anisotropy index. Samples with the addition of enzyme and air exhibit a more distinctive trend. As the shear rate increases, both $E_{\parallel}$ and $E_{\perp}$ increases in Fig. 8b. They reach the largest value at 75 rpm and start to decrease from 75 to 150 rpm, suggesting higher shear rate breaks the fibres. Increasing shear time leads to a continuous increase of Young's moduli. The resultant anisotropy index shown in Fig. 8c almost doubled between samples sheared for 1 and 15 min. Higher anisotropy indices in Fig. 8b and c thus confirm that air bubbles and enzymatic crosslinking are beneficial to the anisotropy at the macroscopic scale (Tian et al., 2018; Wang, Dekkers, Boom, and van der Goot, 2019).

It is interesting to note that $E_{\perp}$ is hardly affected by the shear rate, time or the addition of enzyme and air. It is $E_{\parallel}$ that is responsible for the increase of the anisotropy index. This seems to suggest that the calcium caseinate aggregates are crosslinked along a preferred direction guided by the shear flow. Such an effect is limited to shear times less than 15 min, since longer shear times could lead to phase separation.

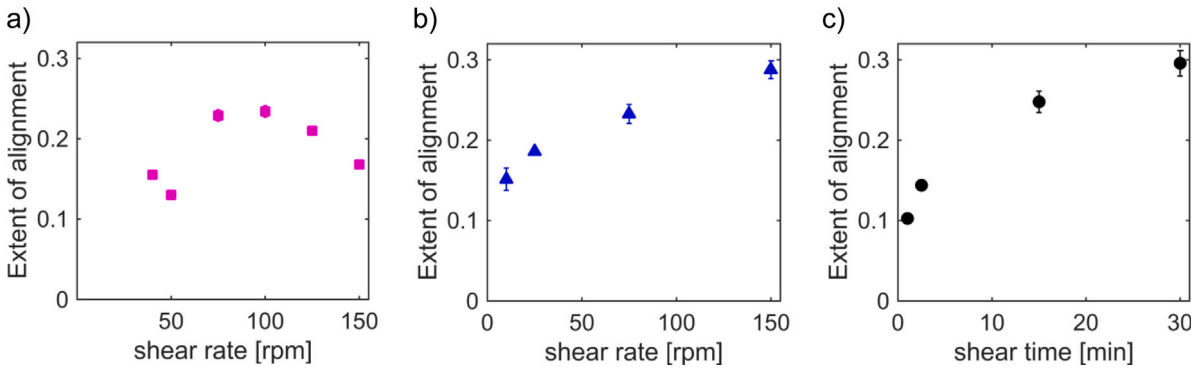

Fig. 7. The extent of alignment of the microfibre as a function of shear rate or time. (a) samples without enzyme or air, sheared at 40, 50, 75, 100, 125 and 150 rpm for 5 min. (b) samples with enzyme and air, sheared at 10, 25, 75 and 150 rpm for 5 min. (c) samples with enzyme and air, sheared at 50 rpm for 1, 2.5, 15 and 30 min.

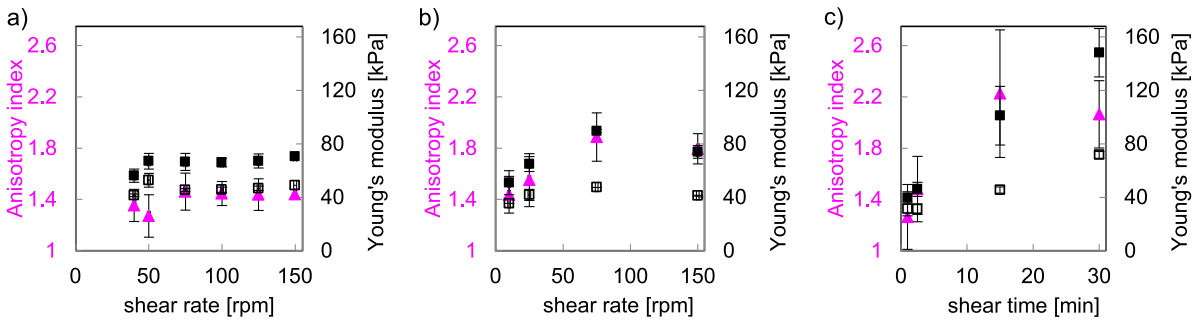

Fig. 8. The anisotropy index (filled triangles) as a function of shear rate or time, the secondary axis is the Young's modulus of samples fractured along (filled squares) or perpendicular (hollow squares) to the shear flow direction. (a) samples without enzyme or air, sheared at 40, 50, 75, 100, 125 and 150 rpm for 5 min. (b) samples with enzyme and air, sheared at 10, 25, 75 and 150 rpm for 5 min. (c) samples with enzyme and air, sheared at 50 rpm for 1, 2.5, 15 and 30 min.

3.4. Discussion

A major interest of this work is to study the correlation between the fibres' extent of alignment at the micro-scale and the mechanical property at the macro-scale. For this purpose, we employed SANS to extract information about the extent of alignment of the micro-fibres from the sub-micron level. For the macroscopic anisotropy, we conducted tensile tests and used the quotient of Young's moduli in two perpendicular directions as an indication.

A comparison between Figs. 7 and 8 shows that the extent of alignment of the micro-fibres and the macroscopic anisotropy index follow the same trend with varying processing conditions. Moreover, the aspect ratio ($=L/D$) of the micro-fibres in Fig. 5 also follows the same trend. The results show that the material possesses a consistent trend in anisotropy at different length scales. These findings imply further that the dimensions of the micro-fibres are responsible for the mechanical property at the macro-scale.

Lastly, calcium caseinate is the only meat analogue candidate, to our knowledge, which displays anisotropy in Young's modulus. Chicken meat also displays anisotropy in Young's modulus (Schreuders, Dekkers, Bodnár, Erni, Boom, & van der Goot, 2019), and it has a fibrous structure at the sub-micron length scale (Tornberg, 2005). In this sense, anisotropy in Young's modulus could be a simple indication of protein alignment at the micro-scale. The only pitfall is that the trend calculated from the Young's moduli can be quite weak, even though the sample displays a clear anisotropy at the microscopic scale, such as the sample set without enzyme or air. This is likely to be caused by the inhomogeneity in the bulk structure, which renders greater uncertainties in the determination of the Young's modulus. Associated errors becomes even larger due to error propagation during calculations of the anisotropy index. It is also worth of mentioning that even though the inhomogeneity poses a challenge to the characterisation of the structure, it does not mean the structure is unsuitable from a food perspective. Indeed, food materials in nature are inherently inhomogeneous, and consumers can in fact prefer and appreciate such an inhomogeneity.

4. Conclusion

To understand the hierarchical structure of the fibres in calcium caseinate, we have conducted SANS measurements quantifying the sizes, structure and extent of alignment of the micro-fibres, and performed tensile tests to study the macroscopic anisotropy of materials processed at different conditions.

Prior to shearing, the protein dispersion is an isotropic gel network loosely formed by sphere-like aggregates. They are composed of sub-aggregates with a mesh size of ~10 nm. Upon shearing, the sphere-like aggregates are aligned and form cylinder-like micro-fibres with a diameter of ~100 nm and a length of ~300 nm. The addition of enzyme and air extends the length of the fibre and decreases its diameter. Enzyme also crosslinks the sub-aggregates and contributes to stronger fibres.

The aspect ratio and the extent of alignment of the micro-fibres follow the same trend with increasing shear rate and time, which means the dimensions of the micro-fibres determine the anisotropy on the sub-micron scale. This microscopic anisotropy is probably also responsible for the anisotropy at the macro-scale, since a similar but weaker trend is observed in the quotient of Young's moduli. The consistency in anisotropy at different length scales thus reveals the relationship between structure and functionality, which can assist in the more rational design of innovative food materials.

In summary, SANS combined with mechanical tests bridge the gap between the macro- and microscopic anisotropy in fibrous calcium caseinate gels. This work has also laid the foundation for characterising dense protein systems that can be explored as candidate materials for future meat analogues.

CRediT authorship contribution statement

Bei Tian: Conceptualization, Visualization, Investigation, Formal analysis, Software, Writing - original draft, Writing - review & editing. **Zhaojun Wang:** Conceptualization, Visualization, Investigation, Formal analysis. **Liliana de Campo:** Data curation, Software, Writing - review & editing. **Elliot P. Gilbert:** Data curation, Software, Writing - review & editing. **Robert M. Dalgliesh:** Data curation, Resources, Investigation, Writing - review & editing. **Evgenii Velichko:** Data curation, Investigation. **Atze Jan van der Goot:** Supervision, Resources, Writing - review & editing. **Wim G. Bouwman:** Supervision, Methodology, Writing - review & editing, Funding acquisition.

Acknowledgements

We gratefully acknowledge the Science and Technology Facilities Council (STFC) for access to neutron beamtime at ISIS through RB1569006 (DOI: 10.5286/ISIS.E.RB1569006); we also acknowledge the support of the ANSTO, in providing access to the BILBY and QUOKKA beamtimes.

This work benefited from the use of the SasView application, originally developed under NSF Award DMR-0520547. SasView also contains code developed with funding from the EU Horizon 2020 programme under the SINE2020 project Grant No 654000.

This work is part of the research project SSCANFoods (project number 13386), which is partly financed by the Netherlands Organisation for Scientific Research (NWO).

Finally, our deep appreciation to Anton Lefering for sending the samples safely to Australia.

Appendix A. Supplementary data

Supplementary material related to this article can be found online at https://doi.org/10.1016/j.foodhyd.2020.105912.

References

Apichartsrangkoon, A. (2002). Dynamic viscoelastic properties of heated gluten/soy protein gels. *Journal of Food Science*, *67*(2), 653–657.

Arnold, O., Bilheux, J. -C., Borreguero, J., Buts, A., Campbell, S. I., Chapon, L., et al. (2014). Mantid–data analysis and visualization package for neutron scattering and μ SR experiments. *Nuclear Instruments and Methods in Physics Research A*, *764*, 156–166.

Asgar, M., Fazilah, A., Huda, N., Bhat, R., & Karim, A. (2010). Nonmeat protein alternatives as meat extenders and meat analogs. *Comprehensive Reviews in Food Science and Food Safety*, *9*(5), 513–529.

Blazek, J., & Gilbert, E. P. (2011). Application of small-angle X-ray and neutron scattering techniques to the characterisation of starch structure: A review. *Carbohydrate Polymers*, *85*(2), 281–293.

Burger, C., Hsiao, B. S., & Chu, B. (2010). Preferred orientation in polymer fiber scattering. *Journal of Macromolecular Science®, Part C: Polymer Reviews*, *50*(1), 91–111.

Curtis, J. E., McAuley, A., Nanda, H., & Krueger, S. (2012). Protein structure and interactions in the solid state studied by small-angle neutron scattering. *Faraday Discussions*, *158*(1), 285–299.

Dalgleish, D. G., Spagnuolo, P. A., & Goff, H. (2004). A possible structure of the casein micelle based on high-resolution field-emission scanning electron microscopy. *International Dairy Journal*, *14*(12), 1025–1031.

De Boer, J., & Aiking, H. (2011). On the merits of plant-based proteins for global food security: marrying macro and micro perspectives. *Ecological Economics*, *70*(7), 1259–1265.

Dekkers, B. L., Hamoen, R., Boom, R. M., & van der Goot, A. J. (2018). Understanding fiber formation in a concentrated soy protein isolate-pectin blend. *Journal of Food Engineering*, *222*, 84–92.

Doucet, M., Cho, J., Alina, G., Bakker, J., Bouwman, W., Butler, P., Washington, A., et al. (2017). Sasview version 4.2.0. http://dx.doi.org/10.5281/zenodo.1412041.

Ducrot, E., Montes, H., & Creton, C. (2015). Structure of tough multiple network elastomers by small angle neutron scattering. *Macromolecules*, *48*(21), 7945–7952.

Elzerman, J. E., van Boekel, M. A., & Luning, P. A. (2013). Exploring meat substitutes: consumer experiences and contextual factors. *British Food Journal*, *115*(5), 700–710.

Elzerman, J. E., Hoek, A. C., Van Boekel, M. A., & Luning, P. A. (2011). Consumer acceptance and appropriateness of meat substitutes in a meal context. *Food Quality and Preference*, *22*(3), 233–240.

Finnigan, T., Needham, L., & Abbott, C. (2017). Mycoprotein: a healthy new protein with a low environmental impact. In *Sustainable protein sources* (pp. 305–325). Elsevier.

Fuquay, J. W., McSweeney, P. L., & Fox, P. F. (2011). *Encyclopedia of dairy sciences*. Academic Press.

Gilbert, E. P. (2019). Small angle X-ray and neutron scattering in food colloids. *Current Opinion in Colloid & Interface Science*, *42*, 55–72.

Gilbert, E. P., Schulz, J. C., & Noakes, T. J. (2006). 'Quokka'—the small-angle neutron scattering instrument at OPAL. *Physica B: Condensed Matter*, *385*, 1180–1182.

Van der Goot, A., Peighambardoust, S., Akkermans, C., & van Oosten-Manski, J. (2008). Creating novel structures in food materials: The role of well-defined shear flow. *Food Biophysics*, *3*(2), 120–125.

Grabowska, K. J., van der Goot, A. J., & Boom, R. M. (2012). Salt-modulated structure formation in a dense calcium caseinate system. *Food Hydrocolloids*, *29*(1), 42–47.

HadjSadok, A., Pitkowski, A., Nicolai, T., Benyahia, L., & Moulai-Mostefa, N. (2008). Characterisation of sodium caseinate as a function of ionic strength, pH and temperature using static and dynamic light scattering. *Food Hydrocolloids*, *22*(8), 1460–1466.

Hammouda, B. (2010). A new guinier–porod model. *Journal of Applied Crystallography*, *43*(4), 716–719.

Hermans, J., Hermans, P., Vermaas, D., & Weidinger, A. (1946). Quantitative evaluation of orientation in cellulose fibres from the X-ray fibre diagram. *Recueil des Travaux Chimiques des Pays-Bas*, *65*(6), 427–447.

Hoek, A. C., Luning, P. A., Weijzen, P., Engels, W., Kok, F. J., & De Graaf, C. (2011). Replacement of meat by meat substitutes. a survey on person-and product-related factors in consumer acceptance. *Appetite*, *56*(3), 662–673.

Ingham, B., Smialowska, A., Erlangga, G. D., Matia-Merino, L., Kirby, N., Wang, C., et al. (2016). Revisiting the interpretation of casein micelle SAXS data. *Soft Matter*, *12*(33), 6937–6953.

Jaspe, J., & Hagen, S. J. (2006). Do protein molecules unfold in a simple shear flow? *Biophysical Journal*, *91*(9), 3415–3424.

Kinney, J., Pople, J., Marshall, G., & Marshall, S. (2001). Collagen orientation and crystallite size in human dentin: a small angle X-ray scattering study. *Calcified Tissue International*, *69*(1), 31–37.

Lopez-Rubio, A., & Gilbert, E. P. (2009). Neutron scattering: a natural tool for food science and technology research. *Trends in Food Science & Technology*, *20*(11–12), 576–586.

Manski, J. M., van der Goot, A. J., & Boom, R. M. (2007). Formation of fibrous materials from dense calcium caseinate dispersions. *Biomacromolecules*, *8*(4), 1271–1279.

Manski, J. M., van Riemsdijk, L. E., van der Goot, A. J., & Boom, R. M. (2007b). Importance of intrinsic properties of dense caseinate dispersions for structure formation. *Biomacromolecules*, *8*(11), 3540–3547.

Martínez-Sanz, M., Gidley, M. J., & Gilbert, E. P. (2015). Application of X-ray and neutron small angle scattering techniques to study the hierarchical structure of plant cell walls: a review. *Carbohydrate polymers*, *125*, 120–134.

Martínez-Sanz, M., Mikkelsen, D., Flanagan, B. M., Gidley, M. J., & Gilbert, E. P. (2017). Multi-scale characterisation of deuterated cellulose composite hydrogels reveals evidence for different interaction mechanisms with arabinoxylan, mixed-linkage glucan and xyloglucan. *Polymer*, *124*, 1–11.

Nieuwland, M., Geerdink, P., Brier, P., Van Den Eijnden, P., Henket, J. T., Langelaan, M. L., et al. (2013). Food-grade electrospinning of proteins. *Innovative Food Science & Emerging Technologies*, *20*, 269–275.

Owusu-Ansah, Y., & McCurdy, S. (1991). Pea proteins: a review of chemistry, technology of production, and utilization. *Food Reviews International*, *7*(1), 103–134.

Peighambardoust, S., Van der Goot, A., Hamer, R., & Boom, R. (2004). A new method to study simple shear processing of wheat gluten-starch mixtures. *Cereal Chemistry*, *81*(6), 714–721.

Saffer, E. M., Lackey, M. A., Griffin, D. M., Kishore, S., Tew, G. N., & Bhatia, S. R. (2014). SANS study of highly resilient poly (ethylene glycol) hydrogels. *Soft Matter*, *10*(12), 1905–1916.

Schmidt, G., Nakatani, A. I., Butler, P. D., & Han, C. C. (2002). Small-angle neutron scattering from viscoelastic polymer- clay solutions. *Macromolecules*, *35*(12), 4725–4732.

Schreuders, F. K., Dekkers, B. L., Bodnár, I., Erni, P., Boom, R. M., & van der Goot, A. J. (2019). Comparing structuring potential of pea and soy protein with gluten for meat analogue preparation. *Journal of Food Engineering*, *261*, 32–39.

Smialowska, A., Matia-Merino, L., Ingham, B., & Carr, A. (2017). Effect of calcium on the aggregation behaviour of caseinates. *Colloid and Surfaces A (Physicochemical and Engineering Aspects)*, *522*, 113–123.

Sokolova, A., Whitten, A. E., de Campo, L., Christoforidis, J., Eltobaji, A., Barnes, J., et al. (2019). Performance and characteristics of the bilby time-of-flight small-angle neutron scattering instrument. *Journal of Applied Crystallography*, *52*(1).

Stothart, P. H., & Cebula, D. J. (1982). Small-angle neutron scattering study of bovine casein micelles and sub-micelles. *Journal of molecular biology*, *160*(2), 391–395.

Thomar, P., Gonzalez-Jordan, A., Dittmer, J., & Nicolai, T. (2017). Effect of orthophosphate and calcium on the self assembly of concentrated sodium caseinate solutions. *International Dairy Journal*, *64*, 1–8.

Thomar, P., Nicolai, T., Benyahia, L., & Durand, D. (2013). Comparative study of the rheology and the structure of sodium and calcium caseinate solutions. *International Dairy Journal*, *31*(2), 100–106.

Tian, B., Wang, Z., van der Goot, A. J., & Bouwman, W. G. (2018). Air bubbles in fibrous caseinate gels investigated by neutron refraction, X-ray tomography and refractive microscope. *Food Hydrocolloids*, *83*, 287–295.

Tornberg, E. (2005). Effects of heat on meat proteins–implications on structure and quality of meat products. *Meat Science*, *70*(3), 493–508.

Wang, Z., Dekkers, B. L., Boom, R., & van der Goot, A. J. (2019). Maltodextrin promotes calcium caseinate fibre formation through air inclusion. *Food Hydrocolloids*, *95*, 143–151.

Wang, Z., Tian, B., Boom, R., & van der Goot, A. J. (2019a). Air bubbles in calcium caseinate fibrous material enhances anisotropy. *Food Hydrocolloids*, *87*, 497–505.

Wang, Z., Tian, B., Boom, R., & van der Goot, A. J. (2019b). Understanding the role of air and protein phase on mechanical anisotropy of calcium caseinate fibers. *Food Research International*, *121*, 862–869.

Weigandt, K. M., Porcar, L., & Pozzo, D. C. (2011). In situ neutron scattering study of structural transitions in fibrin networks under shear deformation. *Soft Matter*, *7*(21), 9992–10000.

Wood, K., Mata, J. P., Garvey, C. J., Wu, C. -M., Hamilton, W. A., Abbeywick, P., et al. (2018). QUOKKA, the pinhole small-angle neutron scattering instrument at the OPAL Research Reactor, Australia: design, performance, operation and scientific highlights. *Journal of Applied Crystallography*, *51*(2), 294–314.

Yokoyama, K., Ohtsuka, T., Kuraishi, C., Ono, K., Kita, Y., Arakawa, T., et al. (2003). Gelation of food protein induced by recombinant microbial transglutaminase. *Journal of Food Science*, *68*(1), 48–51.

Van der Zalm, E., Berghout, J., Van der Goot, A., & Boom, R. (2012). Starch–gluten separation by shearing: Influence of the device geometry. *Chemical Engineering Science*, *73*, 421–430.